







# Forecasting Constraint on Primordial Black Hole Properties with the CSST $3 \times 2$ pt Analysis

Dingao Hu <sup>a,b</sup>, Yan Gong <sup>a,b,c,1</sup>, Pengfei Su,<sup>a,b</sup> Hengjie Lin <sup>a</sup>,  
Haitao Miao <sup>a</sup>, Qi Xiong <sup>a,b</sup> and Xuelei Chen <sup>a,b,d,e,f</sup>

<sup>a</sup>National Astronomical Observatories, Chinese Academy of Sciences, Beijing, 100101, China

<sup>b</sup>School of Astronomy and Space Sciences, University of Chinese Academy of Sciences, Beijing, 100049, China

<sup>c</sup>Science Center for Chinese Space Station Survey Telescope, National Astronomical Observatories, Chinese Academy of Science, Beijing 100101, China

<sup>d</sup>Department of Physics, College of Sciences, Northeastern University, Shenyang 110819, China

<sup>e</sup>Centre for High Energy Physics, Peking University, Beijing 100871, China

<sup>f</sup>State Key Laboratory of Radio Astronomy and Technology, China

E-mail: [huda@bao.an.cn](mailto:huda@bao.an.cn), [gongyan@bao.ac.cn](mailto:gongyan@bao.ac.cn), [supf@bao.ac.cn](mailto:supf@bao.ac.cn), [xuelei@bao.ac.cn](mailto:xuelei@bao.ac.cn)

**Abstract.** This study forecasts the constraints on the properties of primordial black holes (PBHs) as a cold dark matter component using the galaxy clustering, weak lensing, and galaxy-galaxy lensing (i.e.  $3 \times 2$ pt) measurements from the upcoming Chinese Space Station Survey Telescope (CSST) photometric survey. Since PBHs formed via gravitational collapse in the early Universe, they can additionally affect the formation and evolution of the cosmic large-scale structure (LSS) through “Poisson” effect. We compute the angular power spectra for PBH- $\Lambda$ CDM cosmology, and generate mock data based on the CSST instrumental and survey design. The Markov Chain Monte Carlo (MCMC) method is employed to constrain the free parameters, such as the product of the PBH fraction and mass  $f_{\text{PBH}}m_{\text{PBH}}$  and other cosmological parameters. The systematic parameters are also included in the fitting process, such as the parameters of baryonic effect, intrinsic alignment, galaxy bias, photometric redshift (photo- $z$ ) calibration, shear calibration, and noise terms. We find that the CSST  $3 \times 2$ pt analysis can achieve tight constraints on  $f_{\text{PBH}}m_{\text{PBH}}$ , with 68% and 95% confidence levels (CLs) reaching  $< 10^{3.9}M_{\odot}$  and  $< 10^{4.7}M_{\odot}$ , respectively. Additionally, the cosmological parameters, e.g.  $\Omega_m$ ,  $\sigma_8$  and  $w$ , can be constrained with the precisions of 3.3%, 1.7%, 13%, respectively. This indicates that the CSST  $3 \times 2$ pt analysis is a powerful tool to advance the PBH dark matter studies in the near future.

---

<sup>1</sup>Corresponding author.

---

## Contents

<b>1</b>	<b>Introduction</b>	<b>1</b>
<b>2</b>	<b>Theoretical model</b>	<b>2</b>
2.1	PBH- $\Lambda$ CDM Power Spectrum	2
2.2	Galaxy Angular Power Spectrum	3
2.3	Shear Power Spectrum	5
2.4	Galaxy-Galaxy Lensing Power Spectrum	8
<b>3</b>	<b>mock data</b>	<b>10</b>
<b>4</b>	<b>constraint and results</b>	<b>10</b>
4.1	Fitting Method	10
4.2	Constraint result	11
<b>5</b>	<b>summary</b>	<b>13</b>
<b>A</b>	<b>constraint results of systematic parameters</b>	<b>13</b>

---

## 1 Introduction

Primordial black holes (PBHs) are believed to form through gravitational collapse of large overdensity regions in the early Universe. Various theories describe the PBH formation, including inhomogeneities during the radiation-dominated era [1], critical collapse [2, 3], etc. Depending on the PBH formation time from  $10^{-43}$  to 1 s, the PBH mass ranges from  $10^{-5}$  gram to  $10^5 M_{\odot}$ . In some theories, the mass of PBHs can even extend to  $10^{22} M_{\odot}$  [4]. Due to their early formation and wide mass range, PBHs can explain various observational effects as cold dark matter (CDM), such as the cross-correlations between the fluctuations in the source-subtracted Cosmic Infrared Background (CIB) and the unresolved Cosmic X-ray Background (CXB) [5, 6], the UV luminosity density of James Webb Space Telescope (JWST) [7], etc. Different methods are used to constrain the properties of PBHs for different mass ranges, including  $\gamma$ -ray background [8] and anisotropies of cosmic microwave background (CMB) [9] for small-mass PBHs, microlensing for solar-mass PBHs [10], and dynamical motions, Lyman- $\alpha$  forest [11], cosmic large-scale structure (LSS) [12], and the combination of CMB and Baryonic Acoustic Oscillation (BAO) [13] for large-mass PBHs.

The combination of galaxy clustering and cosmic shear measurements, i.e.  $3 \times 2$ pt, is a powerful probe for the LSS, which is widely used to constrain the cosmological parameters [14, 15], including the Kilo-Degree Survey (KiDS)[16, 17], Dark Energy Survey (DES) [15, 18], Hyper Suprime-Cam (HSC) [19, 20], etc. Especially, the upcoming Stage IV surveys can cover larger redshift range and sky area, and will constrain cosmological parameters more tightly, include the Chinese Space Station Survey Telescope (CSST) [21–25], Vera Rubin Observatory’s Legacy Survey of Space and Time (LSST) [26], *Euclid* [27, 28], and Nancy Grace Roman Space Telescope (RST)[29].

In this work, we use the CSST  $3 \times 2$ pt probe to constrain the PBH properties. The CSST is a 2-meter space telescope and will co-orbits with the China Manned Space Station.

It is planned to launch around 2027, and will cover a sky area of  $17500 \text{ deg}^2$  in about ten years with field of view of  $1.1 \text{ deg}^2$ . The CSST can effectively constrain the dark energy and dark matter properties [23, 30–33], neutrino mass [34], ultralight axions [35], modified gravity models [36, 37], etc. The great observational ability of the CSST will also have significant potential for constraining the PBH properties.

The paper is organized as follows: in Section 2, we discuss the PBH effects in cosmology and the theory of angular power spectra for galaxy clusters and cosmic shear; in Section 3, we introduce the method of generating and selecting the mock data of angular power spectra; in Section 4, we discuss the  $3 \times 2$ pt fitting method and constraint results of the free parameters; Section 5 gives the summary and relevant discussions. We assume a flat  $\Lambda$ CDM cosmology with the fiducial values of the cosmological parameters from *Planck* measurements [38].

## 2 Theoretical model

### 2.1 PBH- $\Lambda$ CDM Power Spectrum

PBHs can be seen as a component of CDM, and could cause specific effects on structure formation through their isocurvature perturbations. Therefore, the properties of PBHs can be constrained by the measurements of cosmic structure formation. The influence of PBHs can be specifically categorized into two types: “Poisson” effect and “Seed” effect. The “Poisson” effect represents the collective influence of multiple PBHs coexisting within a given region, and the “Seed” effect represents the isolated influence of a single PBH within a given region [39]. Since there is still no reliable model to accurately describe the “Seed” effect, we only focus on the “Poisson” effect in this work. Regarding the mass spectrum of PBHs, it has been shown that constraints on a monochromatic mass spectrum can be extended to arbitrary mass spectra [40]. Therefore, in this work, we assume that PBHs have a monochromatic mass spectrum.

Under these assumptions, the initial matter power spectrum for PBH isocurvature perturbations is given by [41]

$$P_{\text{PBH}}^{\text{iso}} = f_{\text{PBH}}^2 \bar{n}_{\text{PBH}}^{-1} = \frac{8\pi G f_{\text{PBH}} m_{\text{PBH}}}{3H_0^2 \Omega_{\text{CDM}}}, \quad (2.1)$$

where  $f_{\text{PBH}}$  is the PBH fraction of CDM,  $m_{\text{PBH}}$  is the mass of a single PBH, and  $\bar{n}_{\text{PBH}}$  is the mean volume number density of PBHs in comoving coordinate system. Since  $f_{\text{PBH}}$  and  $m_{\text{PBH}}$  are completely degenerate, the product  $f_{\text{PBH}} m_{\text{PBH}}$  is treated as a free parameter in our analysis.  $\Omega_{\text{CDM}} = \Omega_m - \Omega_b$  is the CDM density parameter, where  $\Omega_m$  and  $\Omega_b$  are the matter and baryon density parameters, respectively. The gravitational constant is  $G = 6.67 \times 10^{-11} \text{ m}^3 \text{ kg}^{-1} \text{ s}^{-2}$  and the Hubble parameter is  $H_0 \equiv 100 h \text{ km s}^{-1} \text{ Mpc}^{-1}$  with  $h = 0.6727$ . Note that the power spectrum of the PBH adiabatic perturbation  $P_{\text{PBH}}^{\text{ad}}$  is identical to that of ordinary CDM, which can be absorbed into the matter power spectrum  $P_{\text{CDM}}^{\text{ad}}$  of the standard  $\Lambda$ CDM [41, 42].

Considering the evolution of PBH isocurvature perturbations and the  $\Lambda$ CDM standard adiabatic model, the total power spectrum of the PBH- $\Lambda$ CDM cosmology can be expressed as

$$P_{\text{tot}}(k, z) = P_{\text{CDM}}^{\text{ad}}(k, z) + D^{\text{iso}}(z)^2 P_{\text{PBH}}^{\text{iso}}, \quad (2.2)$$

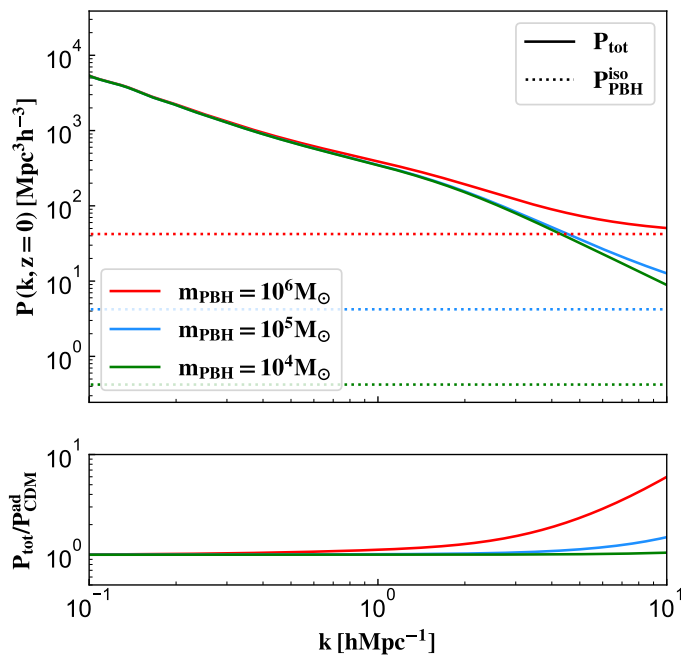


**Figure 1.** The total PBH- $\Lambda$ CDM power spectra (solid curves) and PBH isocurvature power spectra (dotted lines) in the PBH- $\Lambda$ CDM model at  $z = 0$  with  $f_{\text{PBH}} = 1$  for the three PBH masses, i.e.  $m_{\text{PBH}} = 10^4$  (green),  $10^5$  (blue), and  $10^6 M_{\odot}$  (red). The ratio of the PBH- $\Lambda$ CDM and  $\Lambda$ CDM matter power spectrum for each  $m_{\text{PBH}}$  is also shown in the lower panel.

where  $D^{\text{iso}}(z)$  is the growth factor for PBH isocurvature perturbations, follows the expression as below [42]

$$D^{\text{iso}}(z) \approx (1 + \frac{3\gamma}{2\alpha_-} s)^{\alpha_-}, \quad s = \frac{1 + z_{\text{eq}}}{1 + z}, \quad (2.3)$$

$$\alpha_- = \frac{1}{4}(\sqrt{1 + 24\gamma} - 1), \quad \gamma = \frac{\Omega_{\text{CDM}}}{\Omega_m},$$

where  $z_{\text{eq}} = 3400$  is the redshift at matter-radiation equality. Since PBHs mainly affect the cosmic structures at small scales, we estimate the non-linear matter power spectrum  $P_{\text{CDM}}^{\text{ad}}(k, z)$  by using **CAMB** [43] with **HMCode-2020** [44].

In Figure 1, we show the total (solid) and PBH (dotted) isocurvature perturbations power spectra in the PBH- $\Lambda$ CDM cosmology for  $m_{\text{PBH}} = 10^4, 10^5$ , and  $10^6 M_{\odot}$  with  $f_{\text{PBH}} = 1$  at  $z = 0$ . We can find that the PBH power spectrum is a constant for each  $m_{\text{PBH}}$ , and can significantly affect the total power spectrum at small scales of the non-linear regime with  $k \gtrsim 0.7$  and  $4 \text{ Mpc}^{-1}h$  for  $m_{\text{PBH}} = 10^6$  and  $10^5 M_{\odot}$ , respectively.

## 2.2 Galaxy Angular Power Spectrum

After obtaining the total matter power spectrum in the PBH- $\Lambda$ CDM cosmology, we can estimate the galaxy angular auto- or cross-power spectrum for the  $i$ -th and  $j$ -th tomographic redshift bins, which is given by

$$\tilde{C}_{\text{gg}}^{ij} = C_{\text{gg}}^{ij} + \frac{\delta_{ij}}{\bar{n}_{\text{g}}^i} + N_{\text{sys}}^{\text{g}}. \quad (2.4)$$

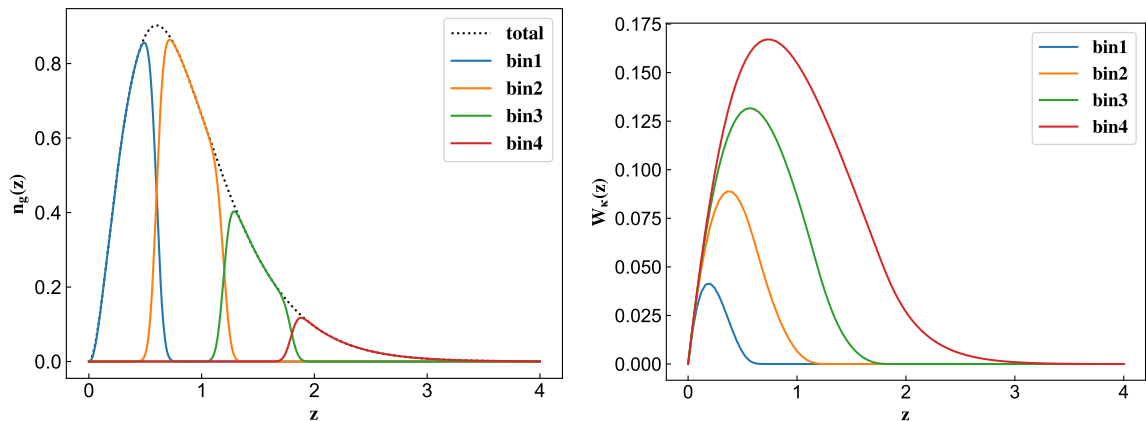


**Figure 2.** *Left panel:* The adopted galaxy redshift distributions in the CSST photometric survey. The black dotted curve shows the normalized total galaxy redshift distribution  $n_g(z)$ , and the blue, orange, green, and red curves denote the galaxy redshift distribution in the four tomographic bins. *Right panel:* The weighting functions of the CSST weak lensing survey for the four tomographic bins.

Here  $\delta_{ij}/\bar{n}_g^i$  represents the shot noise term, where  $\delta_{ij}$  is Kronecker delta function and  $\bar{n}_g^i$  is the mean galaxy surface number density in the  $i$ -th bin.  $N_{\text{sys}}^g$  denotes the systematic error term, which is simply assumed to be independent of bins or scales and can be seen as an average value, and we take  $N_{\text{sys}}^g = 10^{-8}$  as the fiducial value [23]. The quantity  $C_{\text{gg}}^{ij}$  is the clustering term of the galaxy angular power spectrum. Using the flat sky assumption and Limber approximation [45], it can be computed as [14]

$$C_{\text{gg}}^{ij}(\ell) = \int dz H(z) \frac{W_g^i(z) W_g^j(z)}{c D_A^2(z)} P_m \left( \frac{\ell + \frac{1}{2}}{D_A(z)}, z \right), \quad (2.5)$$

where  $c$  is the speed of light,  $H(z)$  is the Hubble parameter,  $D_A$  is the comoving angular diameter distance,  $P_m(k, z) = P_{\text{tot}}(k, z)$  is the total matter power spectrum in the PBH- $\Lambda$ CDM cosmology in our analysis.  $W_g^i(z)$  is the galaxy weight kernel for the  $i$ -th bin, which is expressed as

$$W_g^i(z) = b_g^i(z) n_g^i(z). \quad (2.6)$$

Here  $b_g^i(z)$  is the galaxy bias, and the fiducial value is calculated by  $b_g^i(z) = 1 + 0.84 z_{\text{cen}}^i$ , where  $z_{\text{cen}}^i$  is the central redshift of the  $i$ -th bin [46]. In the fitting process, we set it as a free parameter in each tomographic bin.  $n_g^i(z)$  is the normalized galaxy redshift distribution in the  $i$ -th bin, which has  $\int n_g^i(z) dz = 1$ .

To estimate  $n_g^i(z)$ , we assume that the total galaxy redshift distribution in the CSST photometric survey follows the function as [34]

$$n_g(z) \propto z^2 e^{-z/z^*}. \quad (2.7)$$

Here  $z^* = z_{\text{peak}}/2 = 0.3$ , where the distribution peak is  $z_{\text{peak}} = 0.6$ . Following [23], to utilize more information from the data, the redshift range is divided into four photometric tomographic bins, and we set the redshift bias  $\Delta z^i = 0$  and redshift scatter  $\sigma_z^i = 0.05$  as the fiducial values for each tomographic bin. These parameters are treated as free parameters during the fitting process.

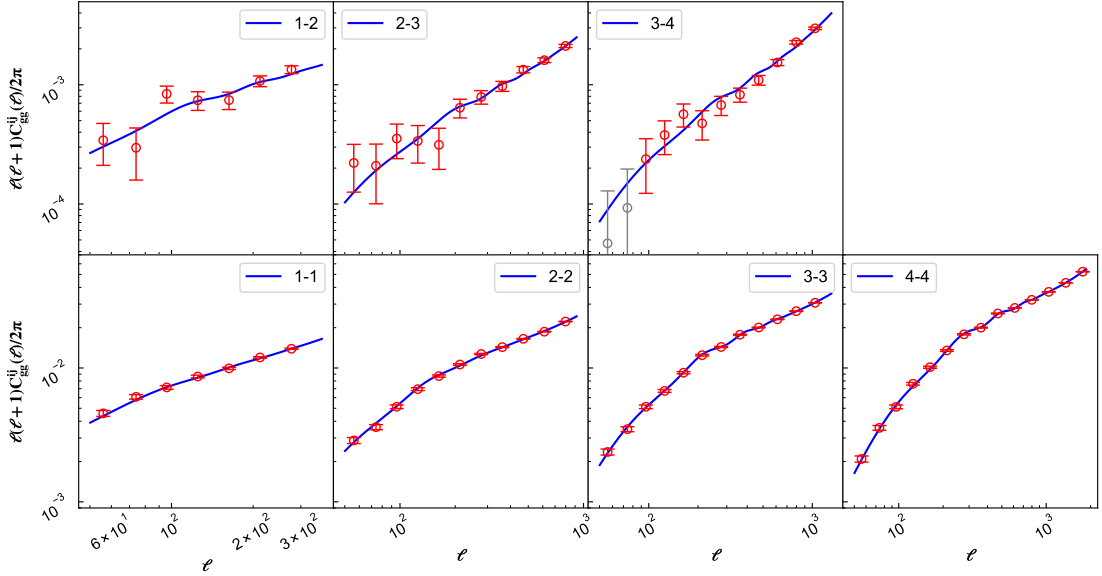


**Figure 3.** The theoretical curves and mock data of the galaxy angular power spectra in different tomographic bins for the CSST  $3\times 2$ pt analysis. The blue solid curves represent the fiducial theoretical predictions. The red data points show the mock data used, while the gray data points indicate the excluded data with the signal-to-noise ratio (SNR)  $< 1$ . Due to the flat sky assumption, Limber approximation and to avoid nonlinear effects, we have set lower and upper limits on  $l$  for different redshift tomography bins. The galaxy cross-power spectra of different tomographic bins with low amplitudes and small overlapping redshift ranges of  $n_g^i(z)$  are also removed.

In the left panel of Figure 2, we show the adopted galaxy redshift distributions. The black dotted curve denotes the total galaxy redshift distribution  $n_g(z)$ , and it is normalized with  $\int n_g(z)dz = 1$ . The colored curves are the galaxy redshift distributions for the four tomographic bins. We find that the mean galaxy surface number densities in the four bins are  $\bar{n}_g^i = 7.9, 11.5, 4.6, 3.7 \text{ arcmin}^{-2}$ , respectively, and the corresponding total number density is  $\bar{n}_g = 27.7 \text{ arcmin}^{-2}$  which is consistent with the previous studies [e.g. 23]. In Figure 3, the blue solid curves denote the theoretical galaxy angular auto- and cross-power spectra for different tomographic bins in the CSST photometric survey.

### 2.3 Shear Power Spectrum

The shear auto- or cross-power spectra measured by the CSST for the  $i$ -th and  $j$ -th bins can be estimated by [e.g. 47]

$$\tilde{C}_{\gamma\gamma}^{ij}(\ell) = (1 + m_i)(1 + m_j)C_{\gamma\gamma}^{ij}(\ell) + \delta_{ij}\frac{\sigma_\gamma^2}{\bar{n}_g^i} + N_{\text{add}}^\gamma, \quad (2.8)$$

where  $\delta_{ij}\sigma_\gamma^2/\bar{n}_g^i$  represents the shape shot noise term,  $\sigma_\gamma^2 = 0.04$  is the shear variance [23]. The quantity  $m_i$  denotes the parameter for the multiplicative error in the  $i$ -th bin. The term  $N_{\text{add}}^\gamma$  is the additive error, which are simply assumed to be independent of bins or scales. We set  $m_i = 0$  and  $N_{\text{add}}^\gamma = 10^{-9}$  as the fiducial values [23]. The shear signal power spectrum is  $C_{\gamma\gamma}^{ij}(\ell)$ , which is given by [48]

$$C_{\gamma\gamma}^{ij} = P_\kappa^{ij}(\ell) + C_{\text{II}}^{ij}(\ell) + C_{\text{GI}}^{ij}(\ell), \quad (2.9)$$

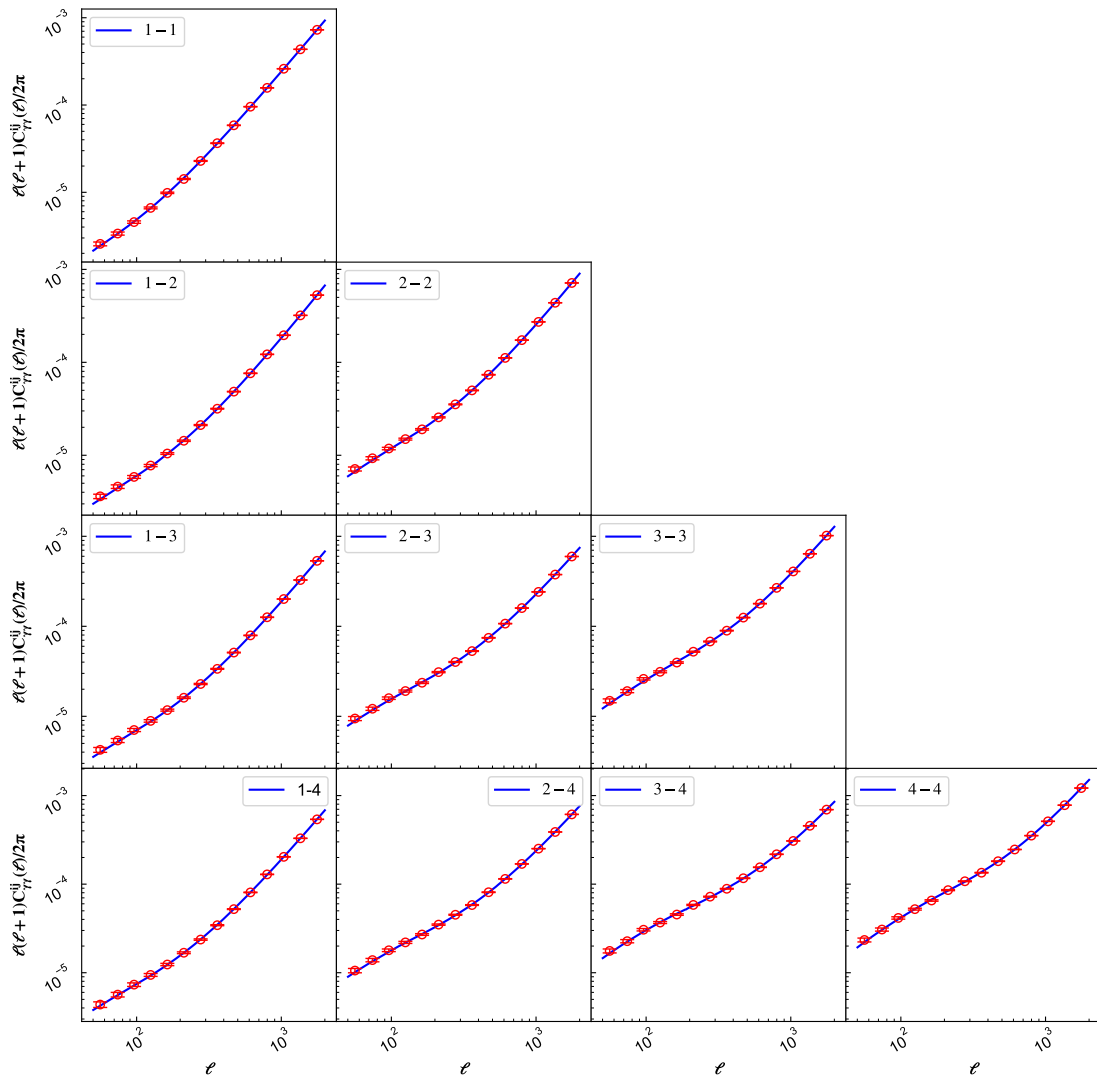


**Figure 4.** The theoretical curves and mock data of the shear angular power spectra for the CSST  $3 \times 2$ pt analysis. The blue solid curves are from the fiducial theoretical models. The red data points show the mock data used. Due to the flat sky assumption and Limber approximation, we have set lower limit on  $l$  for different redshift tomography bins.

where  $P_{\kappa}^{ij}(\ell)$  is the convergence power spectrum, which is the desired signal for cosmological analysis,  $C_{\text{II}}^{ij}(\ell)$  is Intrinsic-Intrinsic power spectrum, which comes from the correlation between the intrinsic ellipticities of two galaxies.  $C_{\text{GI}}^{ij}(\ell)$  is the Gravitational-Intrinsic power spectrum, which arises from the correlations between the gravitational shear of one galaxy and the intrinsic shape of another galaxy [49].

Assuming a flat sky and the Limber approximation [45], the convergence power spectrum  $P_{\kappa}^{ij}(\ell)$  is given by [14]

$$P_{\kappa}^{ij}(\ell) = \int dz H(z) \frac{W_{\kappa}^i(z) W_{\kappa}^j(z)}{c D_A^2(z)} P_m\left(\frac{\ell + \frac{1}{2}}{D_A(z)}, z\right), \quad (2.10)$$

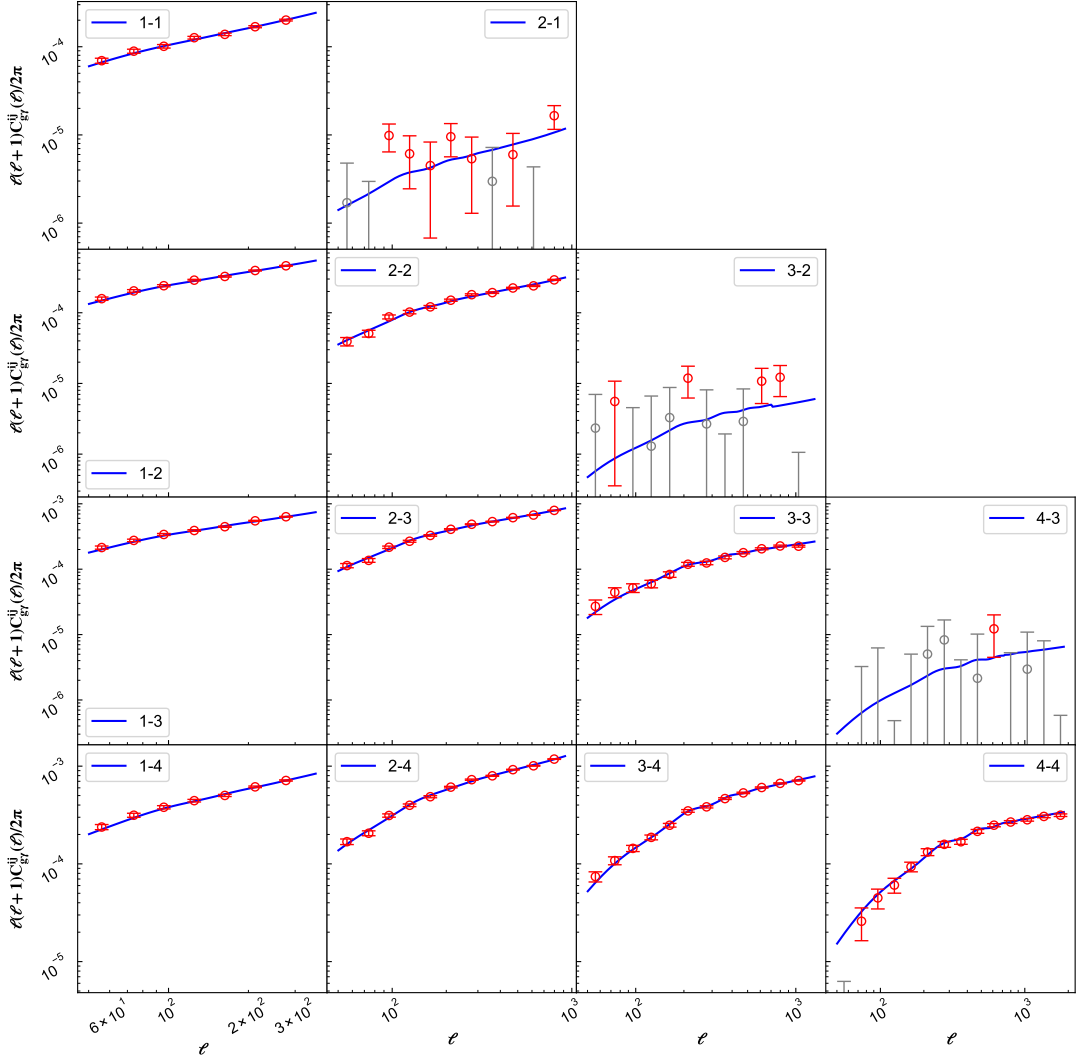


**Figure 5.** The theoretical curves and mock data of the galaxy-galaxy lensing angular power spectra in different tomographic bins for the CSST  $3 \times 2$ pt analysis. The blue solid curves represent the fiducial theoretical predictions. The red data points show the mock data used, while the gray data points indicate the excluded data with the  $\text{SNR} < 1$ . Due to the flat sky assumption, Limber approximation and to avoid nonlinear effects, we have set lower and upper limits on  $l$  for different redshift tomography bins. The galaxy-galaxy lensing cross-power spectra of different tomographic bins with low amplitudes and small overlapping redshift ranges of  $n_g^i(z)$  and  $W_\kappa^i(z)$  are also removed.

where  $W_\kappa^i(z)$  is the lensing kernel function of the  $i$ -th bin, and it can be estimated by

$$W_\kappa^i(z) = \frac{3\Omega_m H_0^2 D_A(z)}{2cH(z)a} \int_z^\infty dz' n_g^i(z') \frac{D_A(z, z')}{D_A(z')}. \quad (2.11)$$

Here the integration limits are from  $z = 0$  to 4. The right panel of Figure 2 shows the lensing weighting kernels for the four bins. We can see that  $W_\kappa^i(z)$  of the high-redshift bins can cover the low-redshift bins, which have wider distributions compared to  $W_\kappa^i(z)$  of the low-redshift bins.

The Intrinsic-Intrinsic power spectrum  $C_{\text{II}}^{ij}(\ell)$  is given by [48]

$$C_{\text{II}}^{ij} = \int dz H(z) \frac{F^i(z)F^j(z)}{cD_{\text{A}}^2(z)} P_m\left(\frac{\ell + 1/2}{D_{\text{A}}(z)}, z\right),$$

$$F^i(z) = A_{\text{IA}} C_1 \rho_c \frac{\Omega_m}{D(z)} n_{\text{g}}^i(z) \left(\frac{1+z}{1+z_0}\right)^{\eta_{\text{IA}}} \left(\frac{L_i}{L_0}\right)^{\beta_{\text{IA}}}. \quad (2.12)$$

Here  $F^i(z)$  is the weighting kernel of the intrinsic alignment effect, the constant  $C_1 = 5 \times 10^{-14} h^{-2} M_{\odot}^{-1} \text{Mpc}^3$ ,  $\rho_c$  represents the present critical density,  $D(z)$  is the linear growth factor,  $z_0$  and  $L_0$  are the pivot redshift and luminosity, and  $A_{\text{IA}}$ ,  $\eta_{\text{IA}}$  and  $\beta_{\text{IA}}$  are free parameters. In this study, we adopt  $z_0 = 0.6$  and set the fiducial values  $A_{\text{IA}} = 1$  and  $\eta_{\text{IA}} = 0$  [48]. For simplicity, we do not consider the luminosity dependence and fix  $\beta_{\text{IA}} = 0$  [23, 34].

The Gravitational-Intrinsic power spectrum consists of two components, representing the cross-correlation between gravitational lensing and intrinsic alignment for the  $i$ -th and  $j$ -th bins, which can be estimated by

$$C_{\text{GI}}^{ij} = \frac{1}{c} \int dz H(z) D_{\text{A}}^{-2}(z) [W^i(z)F^j(z) + W^j(z)F^i(z)] P_m\left(\frac{\ell + 1/2}{D_{\text{A}}(z)}, z\right). \quad (2.13)$$

We find that the relationship  $C_{\gamma\gamma} > C_{\text{GI}} > C_{\text{II}}$  holds, and the effect of PBHs becomes significant when  $l \gtrsim 10^3$ . In Figure 4, the blue solid curves denote the theoretical shear angular auto- and cross-power spectra for different tomographic bins in the CSST photometric survey.

## 2.4 Galaxy-Galaxy Lensing Power Spectrum

The galaxy-galaxy lensing power spectrum represents the cross correlation between the galaxy and weak lensing. It is expressed as [18]

$$C_{\text{g}\gamma}^{ij}(\ell) = C_{\text{g}\kappa}^{ij}(\ell) + C_{\text{gI}}^{ij}(\ell). \quad (2.14)$$

The first term corresponds to the cross-correlation between galaxies and cosmic shear, and the second term is for the cross-correlation between galaxies and intrinsic alignment. The expressions for  $C_{\text{g}\kappa}^{ij}(\ell)$  and  $C_{\text{gI}}^{ij}(\ell)$  are

$$C_{\text{g}\kappa}^{ij}(\ell) = \int dz H(z) \frac{W_{\text{g}}^i(z)W_{\kappa}^j(z)}{cD_{\text{A}}^2(z)} P_m\left(\frac{\ell + 1/2}{D_{\text{A}}(z)}, z\right),$$

$$C_{\text{gI}}^{ij}(\ell) = \int dz H(z) \frac{W_{\text{g}}^i(z)F^j(z)}{cD_{\text{A}}^2(z)} P_m\left(\frac{\ell + 1/2}{D_{\text{A}}(z)}, z\right). \quad (2.15)$$

Since the cross-correlation between galaxy and cosmic shear  $C_{\text{g}\kappa}^{ij}(\ell)$  exceeds that between galaxy and intrinsic alignment  $C_{\text{gI}}^{ij}(\ell)$ ,  $C_{\text{g}\kappa}^{ij}(\ell)$  dominates the total signal. We find that the effect of PBHs becomes significant when  $l \gtrsim 10^3$ . In Figure 5, the blue solid curves denote the theoretical galaxy-galaxy lensing power spectra for different tomographic bins in the CSST photometric survey.

**Table 1.** The fiducial values, priors, best-fitting values and  $1\sigma$  errors of the free parameters in the CSST photometric surveys. The uniform and Gaussian priors are denoted by  $U(a, b)$  and  $N(\mu, \sigma)$ , respectively, where  $a$  and  $b$  are the prior range and  $\mu$  and  $\sigma$  are the mean and standard deviation. The relative accuracy for each parameter is also provided in brackets.

Parameter	Fiducial Value	Prior	Constraints by		
			Galaxy Clustering	Weak Lensing	$3 \times 2$ pt
<b>Cosmological Parameter</b>					
$\Omega_m$	0.32	U(0.2,0.4)	$0.334^{+0.030}_{-0.031}$ (9.2%)	$0.312^{+0.026}_{-0.025}$ (8.2%)	$0.313^{+0.011}_{-0.010}$ (3.3%)
$\Omega_b$	0.048	U(0.01,0.09)	$0.0505^{+0.0068}_{-0.0068}$ (13%)	$0.040^{+0.014}_{-0.014}$ (34%)	$0.0500^{+0.0028}_{-0.0028}$ (5.6%)
$h$	0.6727	N(0.6727,0.0060)	$0.6732^{+0.0057}_{-0.0058}$ (0.85%)	$0.6731^{+0.0059}_{-0.0060}$ (0.89%)	$0.6729^{+0.0055}_{-0.0058}$ (0.84%)
$n_s$	0.96	U(0.85,1.15)	$0.947^{+0.039}_{-0.038}$ (4.0%)	$0.927^{+0.049}_{-0.048}$ (5.2%)	$0.980^{+0.020}_{-0.022}$ (2.1%)
$w$	-1	U(-1.5,0.8)	$-1.10^{+0.20}_{-0.25}$ (21%)	$-1.10^{+0.18}_{-0.13}$ (14%)	$-1.20^{+0.15}_{-0.17}$ (13%)
$\sigma_8$	0.8	U(0.7,0.9)	$0.790^{+0.037}_{-0.031}$ (4.3%)	$0.804^{+0.021}_{-0.022}$ (2.6%)	$0.805^{+0.015}_{-0.012}$ (1.7%)
$\log_{10}(f_{\text{PBH}} m_{\text{PBH}}^+ 1)$	0	U[0,8)	< 4.6	< 4.1	< 3.9
<b>Baryonic Effect</b>					
$\log_{10}(T_{\text{AGN}}/K)$	7.8	U(7.0,8.3)	$7.53^{+0.43}_{-0.35}$ (5.2%)	$7.60^{+0.17}_{-0.13}$ (2.0%)	$7.756^{+0.094}_{-0.093}$ (1.2%)
<b>Intrinsic Alignment</b>					
$A_{\text{IA}}$	1	U(-5,5)	—	$1.04^{+0.23}_{-0.17}$ (19%)	$0.968^{+0.041}_{-0.036}$ (4.0%)
$\eta_{\text{IA}}$	0	U(-5,5)	—	$-0.03^{+0.82}_{-0.72}$	$0.144^{+0.085}_{-0.087}$
<b>Galaxy Bias</b>					
$b^1$	1.252	U(0,5)	$1.221^{+0.071}_{-0.068}$	—	$1.242^{+0.022}_{-0.024}$
$b^2$	1.756	U(0,5)	$1.777^{+0.069}_{-0.076}$	—	$1.767^{+0.037}_{-0.036}$
$b^3$	2.260	U(0,5)	$2.31^{+0.10}_{-0.10}$	—	$2.306^{+0.062}_{-0.061}$
$b^4$	3.436	U(0,5)	$3.49^{+0.18}_{-0.18}$	—	$3.50^{+0.11}_{-0.11}$
<b>Photo-<math>z</math> Calibration</b>					
$\Delta z^1$	0	U(-0.1,0.1)	$-0.027^{+0.047}_{-0.040}$	$-0.000^{+0.022}_{-0.034}$	$-0.0074^{+0.0077}_{-0.0097}$
$\Delta z^2$	0	U(-0.1,0.1)	$-0.018^{+0.040}_{-0.035}$	$0.005^{+0.026}_{-0.036}$	$-0.0073^{+0.0081}_{-0.0010}$
$\Delta z^3$	0	U(-0.1,0.1)	$-0.011^{+0.041}_{-0.038}$	$0.004^{+0.036}_{-0.034}$	$-0.008^{+0.011}_{-0.014}$
$\Delta z^4$	0	U(-0.1,0.1)	$-0.010^{+0.052}_{-0.046}$	$0.023^{+0.052}_{-0.055}$	$-0.016^{+0.017}_{-0.018}$
$\sigma_z^1/\sigma_{z,\text{fid}}^1$	1	U(0.5,1.5)	$1.00^{+0.32}_{-0.33}$	$1.05^{+0.31}_{-0.36}$	$1.0^{+0.1}_{-0.1}$
$\sigma_z^2/\sigma_{z,\text{fid}}^2$	1	U(0.5,1.5)	$1.02^{+0.32}_{-0.35}$	$1.06^{+0.31}_{-0.33}$	$0.957^{+0.060}_{-0.074}$
$\sigma_z^3/\sigma_{z,\text{fid}}^3$	1	U(0.5,1.5)	$1.03^{+0.31}_{-0.34}$	$0.99^{+0.35}_{-0.33}$	$0.976^{+0.095}_{-0.093}$
$\sigma_z^4/\sigma_{z,\text{fid}}^4$	1	U(0.5,1.5)	$0.87^{+0.52}_{-0.47}$	$0.97^{+0.34}_{-0.33}$	$0.82^{+0.25}_{-0.20}$
<b>Shear Calibration and Noise</b>					
$m_1$	0	U(-0.1,0.1)	—	$0.008^{+0.054}_{-0.055}$	$0.027^{+0.037}_{-0.036}$
$m_2$	0	U(-0.1,0.1)	—	$0.011^{+0.050}_{-0.054}$	$0.019^{+0.032}_{-0.033}$
$m_3$	0	U(-0.1,0.1)	—	$0.013^{+0.048}_{-0.052}$	$0.021^{+0.032}_{-0.033}$
$m_4$	0	U(-0.1,0.1)	—	$0.010^{+0.047}_{-0.054}$	$0.023^{+0.032}_{-0.033}$
$N_{\text{sys}}^g$	$10^{-8}$	$U(0.5, 1.5) \times 10^{-8}$	$1.063^{+0.043}_{-0.042} \times 10^{-8}$	—	$9.93^{+0.26}_{-0.28} \times 10^{-9}$
$N_{\text{add}}^\gamma$	$10^{-9}$	$U(0.5, 1.5) \times 10^{-9}$	—	$9.987^{+0.027}_{-0.025} \times 10^{-10}$	$1.0032^{+0.0021}_{-0.0024} \times 10^{-9}$
$N_{\text{add}}^{g\gamma}$	0	$U(-1, 1) \times 10^{-8}$	—	—	$0.1^{+1.4}_{-1.4} \times 10^{-11}$

### 3 mock data

To generate the mock data of the CSST  $3 \times 2$ pt probe, the covariance matrix is needed, which can be estimated by [14]

$$\text{Cov}[\tilde{C}_{xy}^{ab}(\ell)\tilde{C}_{mn}^{ij}(\ell')] = \frac{\delta_{\ell\ell'}}{(2\ell+1)f_{\text{sky}}\Delta\ell}[\tilde{C}_{xm}^{ai}(\ell)\tilde{C}_{yn}^{bj}(\ell) + \tilde{C}_{xn}^{aj}(\ell)\tilde{C}_{ym}^{bi}(\ell)], \quad (3.1)$$

where  $a, b, i, j \in \{1, 2, 3, 4\}$  denote different tomographic bins, and  $x, y, m, n \in \{g, \gamma\}$  denote galaxy or shear.  $f_{\text{sky}} \simeq 0.42$  is the sky fraction for the CSST wide-field survey. The covariance matrix is decomposed using Cholesky decomposition. Then, it is multiplied by a standard normal random matrix. This yields a random displacement matrix with the same covariance. The random displacement data are added to the  $3 \times 2$ pt theoretical predictions and forms the  $3 \times 2$  pt mock observed data. The mock data points of the CSST galaxy, weak lensing, and galaxy-lensing power spectra are shown in Figure 3, Figure 4, and Figure 5, respectively. The error bars of the data points in these figures are derived from the diagonal components of the covariance matrix.

Since the flat sky assumption and Limber approximation are only valid at  $l \gtrsim 50$  [45], the data points of the angular power spectra at  $l < 50$  are discarded in the fitting process. Besides, we only adopt the data points with  $\text{SNR} > 1$  to improve the data quality and reduce computational time. The data points at small scales in the non-linear regime with  $k > 0.3 \text{ Mpc}^{-1}h$  are also removed in the galaxy and galaxy-lensing power spectra, which corresponds to  $l_{\text{max}} = 359, 920, 1316, 1891$  [34]. For the shear power spectra, we take  $l_{\text{max}} = 2000$ . In addition, we also discard the cross power spectra of different tomographic bins for galaxies and shear signals with low amplitudes in Figure 3 and Figure 5, which have small overlapping redshift ranges for  $n_g^i(z)$ , or  $n_g^i(z)$  and  $W_\kappa^i(z)$ , as shown in Figure 2.

## 4 constraint and results

### 4.1 Fitting Method

We adopt the  $\chi^2$  method to fit the mock data, which is given by

$$\chi^2 = [\mathbf{D} - \mathbf{T}]^T \mathbf{Cov}^{-1} [\mathbf{D} - \mathbf{T}], \quad (4.1)$$

where  $\mathbf{D}$  represents the  $3 \times 2$ pt data vector,  $\mathbf{T}$  is the corresponding theoretical prediction vector, and  $\mathbf{Cov}$  is the corresponding covariance matrix. The likelihood function follows  $\mathcal{L} \sim \exp(-\chi^2/2)$ .

The fitting process uses the `emcee` [50] package, which implements an Markov Chain Monte Carlo (MCMC) ensemble sampler. In Table 1, we summarize the free parameters, their fiducial values and priors for the CSST galaxy clustering, weak lensing, and  $3 \times 2$ pt surveys. The PBH parameter  $f_{\text{PBH}}m_{\text{PBH}}$  spans nearly ten orders of magnitude, and thus its logarithmic form is taken, i.e.  $\log_{10}(f_{\text{PBH}}m_{\text{PBH}} + 1)$  as the constraint parameter. The MCMC implementation uses 150 walkers with 22,000 steps each to ensure the convergence. After burn-in and thinning process, approximately 10,000 chain points remain to illustrate the 1D probability distribution functions (PDFs) and contour maps of the free parameters.

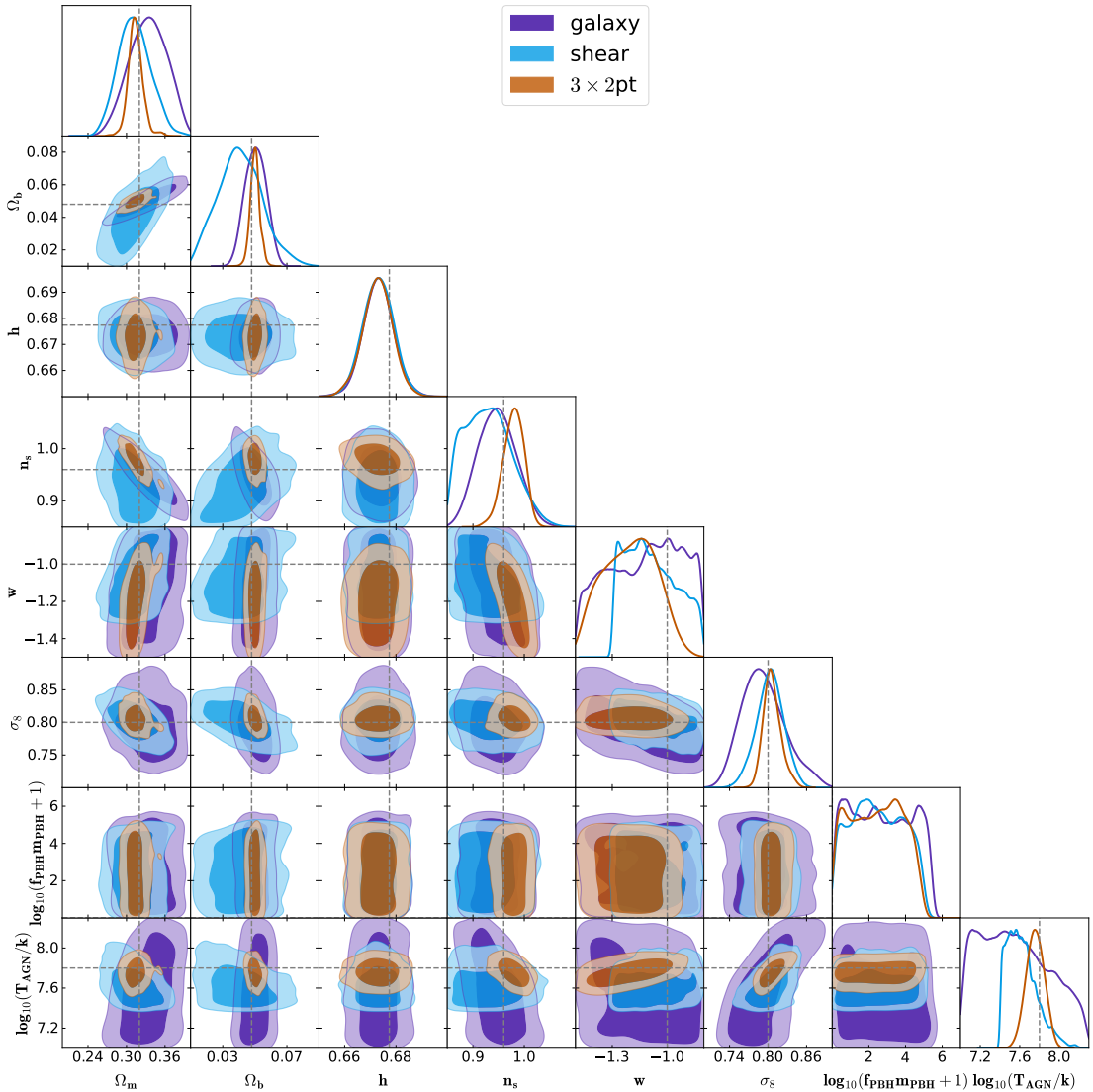


**Figure 6.** The contour maps with  $1\sigma$  (68%) and  $2\sigma$  (95%) CLs and 1D PDFs of the cosmological, PBH, and baryonic effect parameters for the CSST galaxy clustering (purple), cosmic shear (blue) and  $3\times 2$ pt (brown) surveys. The gray vertical and horizontal dashed lines indicate the fiducial values of these parameters.

## 4.2 Constraint result

In Figure 6, the contour maps and 1D PDFs for the PBH, cosmological, and baryonic effect parameters have been shown. The  $1\sigma$  constraint result and the relative constraint accuracy for each parameter from the CSST galaxy clustering, weak lensing, and  $3\times 2$ pt surveys are listed in Table 1.

We can find that, due to the large sky area and redshift coverage of the CSST photometric survey, the constraint accuracies of the PBH parameter product  $f_{\text{PBH}}m_{\text{PBH}}$  can reach  $< 10^{3.9}M_{\odot}$  and  $< 10^{4.7}M_{\odot}$  for  $1\sigma$  and  $2\sigma$  confidence levels (CLs), respectively. We also notice that the constraint on the product  $f_{\text{PBH}}m_{\text{PBH}}$  from the CSST  $3\times 2$ pt analysis is similar to that from the CSST weak lensing survey, which indicates that the constraint power is mainly

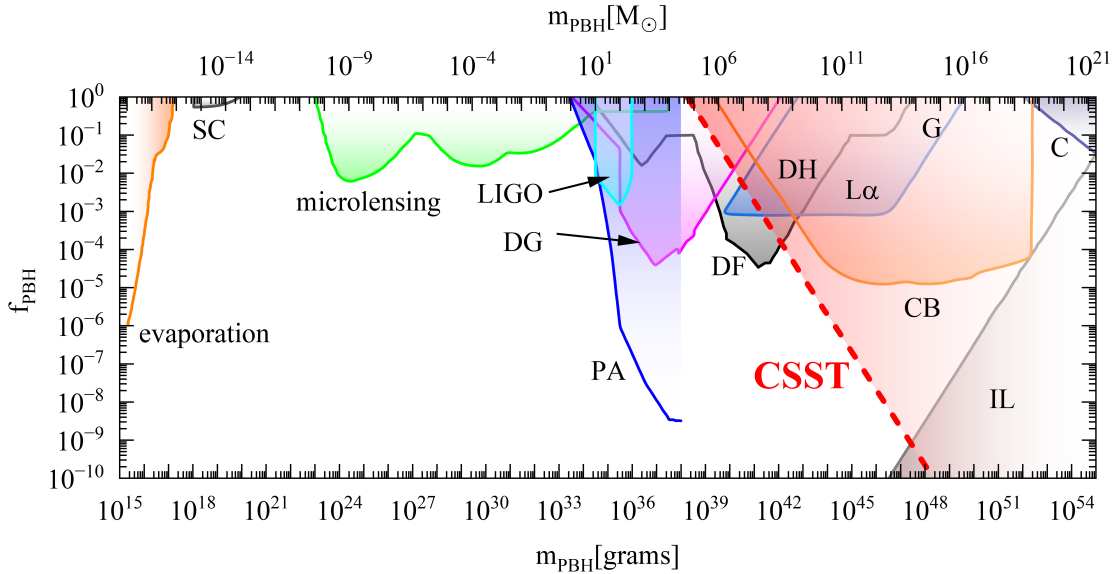


**Figure 7.** Comparison of the constraints on the monochromatic mass function  $f_{\text{PBH}}(m_{\text{PBH}})$ . The filled regions represent the excluded parameter space. The red dash line is derived from the  $2\sigma$  upper limit ( $f_{\text{PBH}}m_{\text{PBH}} < 10^{4.7}M_{\odot}$ ) given by this work using the CSST  $3 \times 2\text{pt}$  analysis. The solid lines indicate various previous constraints, including the limits from evaporation (orange), microlensing (green), Planck measurements of CMB distortions (PA, blue), halo dynamical friction (DF, black), heating of stars in the Galactic disk (DH, black), galaxy tidal distortions (G, black), CMB dipole (CMB, navy blue), and incredulity limits (IL, burgundy) [51]. Additional constraints come from PBH capture by stars (SC, gray)[52], LIGO observation of the merger rate of PBH binaries (LIGO, cyan) [53], PBH in the halos of dwarf galaxies (DG, magenta) [54], Lyman- $\alpha$  forest ( $L\alpha$ , sky blue) [11], and the combination of CMB and BAO (CB, orange) [13].

provided by the CSST shear measurement covering the small scales.

In Figure 7, we show the comparison of the constraint on  $f_{\text{PBH}}$  as a function of  $m_{\text{PBH}}$  with other results, based on our  $2\sigma$  upper limit with  $f_{\text{PBH}}m_{\text{PBH}} < 10^{4.7}M_{\odot}$ . The filled regions represent the excluded parameter space. In the mass range  $m_{\text{PBH}} \gtrsim 10^8M_{\odot}$ , we can see that the CSST  $3 \times 2\text{pt}$  analysis can provide tighter constraints than other current methods, such as  $L\alpha$ , CB, DH, and CMB, especially in the mass range  $10^{14}M_{\odot} < m_{\text{PBH}} < 10^{18}M_{\odot}$  where currently there is only one effective constraint. Therefore, it demonstrates strong potential for the future studies of massive PBHs using the CSST  $3 \times 2\text{pt}$  analysis.

For the cosmological parameters, e.g.  $\Omega_m$ ,  $\sigma_8$ , and  $w$ , we find that the CSST  $3 \times 2\text{pt}$  analysis can provide the constraint accuracies  $\sim 3.3\%$ ,  $1.7\%$ , and  $13\%$ , respectively, which are much more stringent than those given by the current similar surveys, e.g. DES [15]. Compared with the previous CSST  $3 \times 2\text{pt}$  forecast [e.g. 34, 35], we notice that the values of relative constraint accuracies of these parameters are larger. This is mainly because that we have included more parameters in this analysis, such as the noise parameters  $N_{\text{sys}}^g$ ,  $N_{\text{add}}^\gamma$ , and  $N_{\text{add}}^{g\gamma}$ .

In addition, we find that the systematical parameters are also correctly constrained in the CSST photometric surveys, and their fiducial values are within the  $1\sigma$  CL, such as the parameters of baryonic effect  $\log_{10}(T_{\text{AGN}}/k)$ , intrinsic alignment  $A_{\text{IA}}$  and  $\eta_{\text{IA}}$ , galaxy bias in each redshift bin  $b_g^i$ , photo- $z$  calibration in each redshift bin  $\Delta z^i$  and  $\sigma_z^i$ , shear calibration in each redshift bin  $m_i$ , and noise terms  $N_{\text{sys}}^g$ ,  $N_{\text{add}}^\gamma$ , and  $N_{\text{add}}^{g\gamma}$ . A detailed discussion of these

parameters is provided in appendix A.

## 5 summary

In this work, we forecast the constraint on the product of the PBH CDM fraction and mass, i.e.  $f_{\text{PBH}}m_{\text{PBH}}$ , and other cosmological parameters using the CSST  $3\times 2$ pt analysis. The modeling incorporates PBH isocurvature perturbations and ordinary  $\Lambda$ CDM adiabatic perturbations to construct the total matter power spectrum and then generate the mock data of the angular power spectra of galaxy clustering, weak lensing, and galaxy-galaxy lensing based on the design of the CSST photometric survey. The systematic parameters of baryonic effect, intrinsic alignment, galaxy bias, photo- $z$  calibration, shear calibration, and noise terms, are also considered and jointly constrained in the MCMC fitting process.

We find that the CSST  $3\times 2$ pt analysis can provide tight constraints on the PBH parameter with  $f_{\text{PBH}}m_{\text{PBH}} < 10^{3.9}M_{\odot}$  and  $< 10^{4.7}M_{\odot}$  for  $1\sigma$  and  $2\sigma$  CLs, respectively. It excludes significant portions of the parameter space in the mass range  $m_{\text{PBH}} > 10^8M_{\odot}$ , especially for  $10^{14}M_{\odot} < m_{\text{PBH}} < 10^{18}M_{\odot}$  where the existing methods lack of sensitivity. We also notice that this constraint is mainly contributed by the CSST weak lensing measurement, which can provide more information at small scales. Besides, the constraints on the cosmological parameters, such as  $\Omega_m$ ,  $\sigma_8$ , and  $w$  can achieve much higher precision compared to the current photometric surveys, and the systematic parameters are also well-constrained. Our results validates the potential of the upcoming or ongoing Stage IV surveys for exploring the LSS evolution of the Universe, and indicates that the CSST  $3\times 2$ pt analysis can be a powerful tool for investigating the properties of PBHs.

## Acknowledgments

D.A.H and Y.G. acknowledge the support from the CAS Project for Young Scientists in Basic Research (No. YSBR-092), and National Key R&D Program of China grant Nos. 2022YFF0503404 and 2020SKA0110402. X.L.C. acknowledges the support of the National Natural Science Foundation of China through grant Nos. 11473044 and 11973047 and the Chinese Academy of Science grants ZDKYYQ20200008, QYZDJ-SSW-SLH017, XDB 23040100, and XDA15020200. This work is also supported by science research grants from the China Manned Space Project with grant Nos. CMS-CSST-2025-A02, CMS-CSST-2021-B01, and CMS-CSST-2021-A01.

## A constraint results of systematic parameters

The CSST photometric survey also can effectively constrain the systematic parameters in the model. In Figure 8 and 9, we show the contour maps and 1D PDFs of the parameters of galaxy bias, intrinsic alignment, multiplicative error, and noise terms in the CSST galaxy clustering, shear, and  $3\times 2$ pt measurements. Compared to the galaxy clustering measurement, the  $3\times 2$ pt analysis can improve the constraint accuracies of the galaxy bias and shot noise by a factor of  $\sim 2$ . For the intrinsic alignment parameters, the  $3\times 2$ pt method demonstrates a significant advantage in constraining  $A_{\text{IA}}$ , improving the constraint accuracy by a factor of  $\sim 5$ . In Figure 10, we show the contour maps and 1D PDFs of the systematic parameters in photo- $z$  calibration, i.e.  $\Delta z^i$  and  $\sigma_z^i$ . Compared to the results from the CSST galaxy clustering only and shear only measurements, the CSST  $3\times 2$ pt survey can improve the constraint accuracy by a factor of  $\sim 3$ .

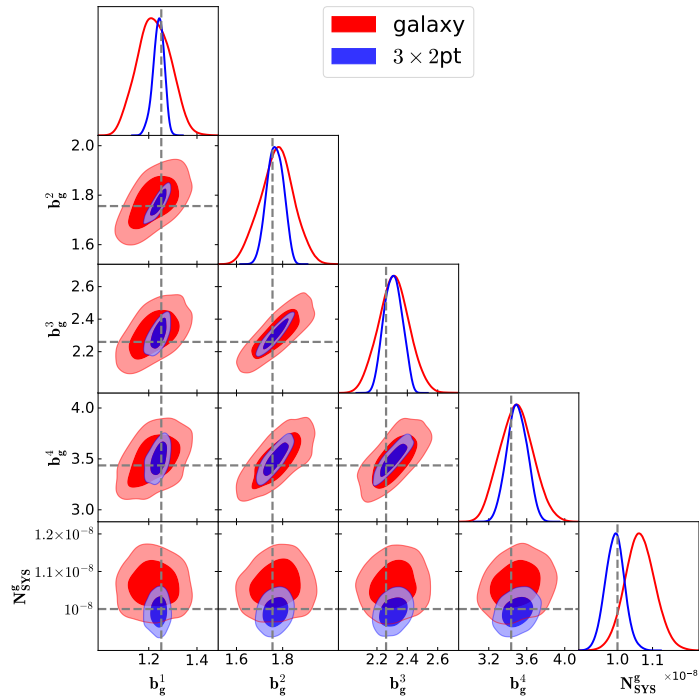


**Figure 8.** The contour maps with  $1\sigma$  and  $2\sigma$  CLs and 1D PDFs of galaxy bias and systematic noise for the CSST galaxy clustering (red) and  $3\times 2$ pt surveys (blue).

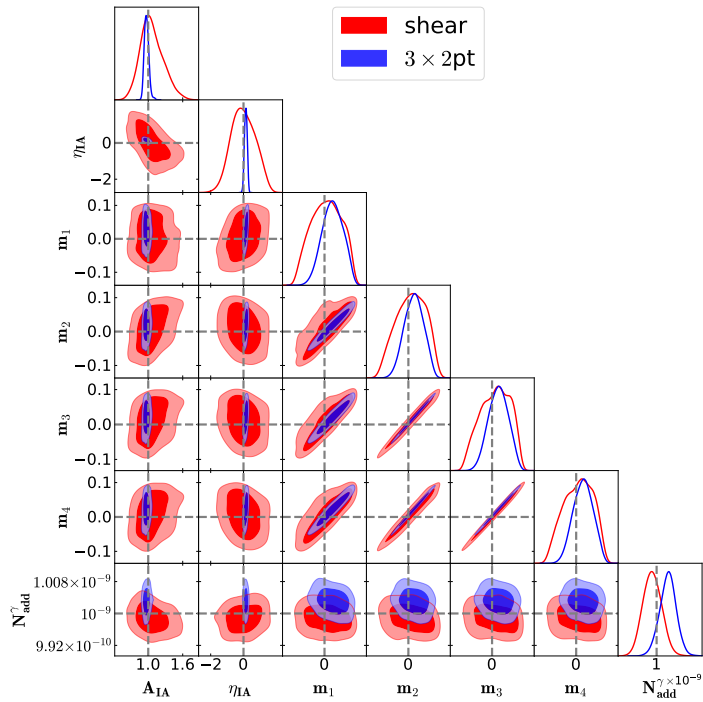


**Figure 9.** The contour maps with  $1\sigma$  and  $2\sigma$  CLs and 1D PDFs of intrinsic alignment, multiplicative and additive errors for the CSST shear (red) and  $3\times 2$ pt surveys (blue). The gray vertical and horizontal dashed lines indicate the fiducial values of these parameters.

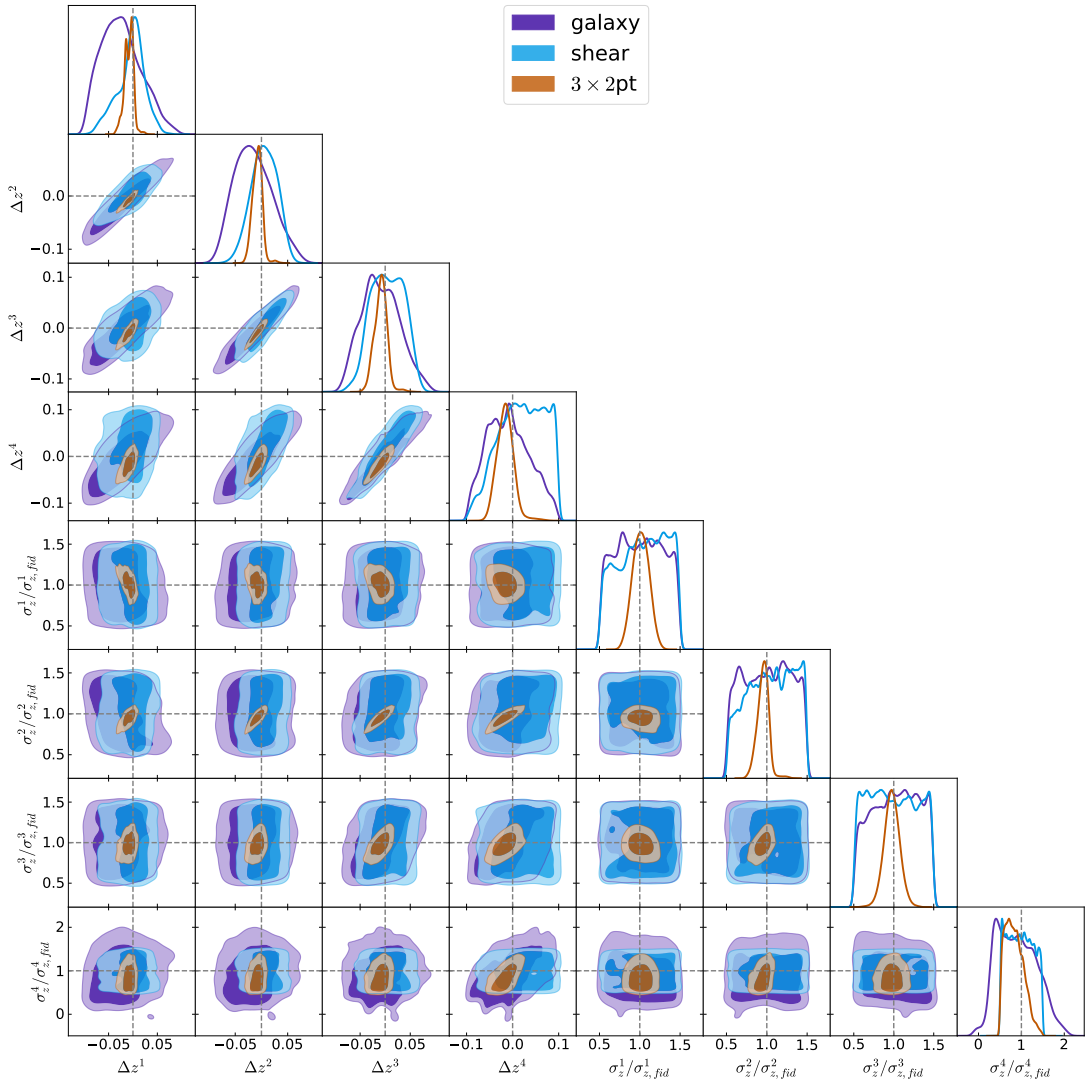


**Figure 10.** The contour maps with  $1\sigma$  and  $2\sigma$  CLs and 1d PDFs of the systematic parameters in the photo- $z$  calibration for the CSST galaxy clustering (purple), cosmic shear (blue) and  $3\times 2$ pt (brown) surveys. The gray vertical and horizontal dashed lines indicate the fiducial values of these parameters.

## References

- [1] B.J. Carr, *The primordial black hole mass spectrum*, *Astrophysical Journal* **201** (1975) 1.
- [2] F. Kühnel, C. Rampf and M. Sandstad, *Effects of critical collapse on primordial black-hole mass spectra*, *The European Physical Journal C* **76** (2016) 93.
- [3] B. Carr, S. Clesse and J. García-Bellido, *Primordial black holes from the QCD epoch: linking dark matter, baryogenesis, and anthropic selection*, *Monthly Notices of the Royal Astronomical Society* **501** (2021) 1426.
- [4] B.J. Carr and A.M. Green, *The history of primordial black holes*, .
- [5] A. Kashlinsky, *LIGO gravitational wave detection, primordial black holes and the near-IR cosmic infrared background anisotropies*, *The Astrophysical Journal* **823** (2016) L25.

- [6] N. Cappelluti, A. Kashlinsky, R. Arendt, A. Comastri, G. Fazio, A. Finoguenov et al., *Cross-correlating cosmic IR and X-ray background fluctuations: evidence of significant black hole populations among the CIB sources*, *The Astrophysical Journal* **769** (2013) 68.
- [7] A. Matteri, A. Ferrara and A. Pallottini, *Beyond the first galaxies primordial black holes shine*, Mar., 2025. 10.48550/arXiv.2503.18850.
- [8] A. Arbey, J. Auffinger and J. Silk, *Constraining primordial black hole masses with the isotropic gamma ray background*, *Physical Review D* **101** (2020) 023010.
- [9] P.D. Serpico, *CMB and accretion*, June, 2024.
- [10] B. Carr, K. Kohri, Y. Sendouda and J. Yokoyama, *Constraints on Primordial Black Holes*, *Reports on Progress in Physics* **84** (2021) 116902.
- [11] M.M. Ivanov and S. Trifinopoulos, *Effective field theory constraints on primordial black holes from the high-redshift lyman- $\alpha$  forest*, .
- [12] C. Byrnes, G. Franciolini, T. Harada, P. Pani and M. Sasaki, eds., *Primordial black holes*, Springer Series in Astrophysics and Cosmology, Springer Nature Singapore, Singapore (2025), 10.1007/978-981-97-8887-3.
- [13] C. Gerlach, Y. Gouttenoire, A.J. Iovino and N. Leister, *Closing the mass window for stupendously large black holes*, .
- [14] W. Hu and B. Jain, *Joint galaxy-lensing observables and the dark energy*, *Physical Review D* **70** (2004) 043009.
- [15] D.E.S. Collaboration, T.M.C. Abbott, M. Aguena, A. Alarcon, S. Allam, O. Alves et al., *Dark energy survey year 3 results: cosmological constraints from galaxy clustering and weak lensing*, *Physical Review D* **105** (2022) 023520.
- [16] B. Stolzner, A.H. Wright, M. Asgari, C. Heymans, H. Hildebrandt, H. Hoekstra et al., *KiDS-legacy: consistency of cosmic shear measurements and joint cosmological constraints with external probes*, .
- [17] A.H. Wright, B. Stolzner, M. Asgari, M. Bilicki, B. Giblin, C. Heymans et al., *KiDS-legacy: cosmological constraints from cosmic shear with the complete kilo-degree survey*, .
- [18] T. Abbott, F. Abdalla, A. Alarcon and others, *Dark energy survey year 1 results: cosmological constraints from galaxy clustering and weak lensing*, *Physical Review D* **98** (2018) 043526.
- [19] S. More, S. Sugiyama, H. Miyatake, M.M. Rau, M. Shirasaki, X. Li et al., *Hyper supprime-cam year 3 results: Measurements of clustering of sdss-boss galaxies, galaxy-galaxy lensing, and cosmic shear*, *Phys. Rev. D* **108** (2023) 123520.
- [20] S. Sugiyama, H. Miyatake, S. More, X. Li, M. Shirasaki, M. Takada et al., *Hyper supprime-cam year 3 results: Cosmology from galaxy clustering and weak lensing with hsc and sdss using the minimal bias model*, *Phys. Rev. D* **108** (2023) 123521.
- [21] H. Zhan, *Consideration for a large-scale multi-color imaging and slitless spectroscopy survey on the chinese space station and its application in dark energy research*, *SCIENTIA SINICA Physica, Mechanica & Astronomica* **41** (2011) 1441.
- [22] H. Zhan, *The wide-field multiband imaging and slitless spectroscopy survey to be carried out by the survey space telescope of China manned space program*, *Chinese Science Bulletin* **66** (2021) 1290.
- [23] Y. Gong, X. Liu, Y. Cao, X. Chen, Z. Fan, R. Li et al., *Cosmology from the Chinese Space Station Optical Survey (CSS-OS)*, *The Astrophysical Journal* **883** (2019) 203.
- [24] Y. Gong, H. Miao, X. Zhou, Q. Xiong, Y. Song, Y. Jiang et al., *Future cosmology: new physics and opportunity from the China space station telescope (CSST)*, *Science China Physics, Mechanics & Astronomy* **68** (2025) 280402.

- [25] C. Collaboration, Y. Gong, H. Miao, H. Zhan, Z.-Y. Li, J. Shangguan et al., *Introduction to the chinese space station survey telescope (CSST)*, Sept., 2025. 10.48550/arXiv.2507.04618.
- [26] Z. Ivezić, S.M. Kahn, J.A. Tyson, B. Abel, E. Acosta, R. Allsman et al., *Lsst: From science drivers to reference design and anticipated data products*, *The Astrophysical Journal* **873** (2019) 111.
- [27] E. Collaboration, L. Blot, K. Tanidis, G. Cañas-Herrera, P. Carrilho, M. Bonici et al., *Euclid preparation. Cosmology likelihood for observables in euclid (CLOE). 6: impact of systematic uncertainties on the cosmological analysis*, .
- [28] E. Collaboration, G. Cañas-Herrera, L.W.K. Goh, L. Blot, M. Bonici, S. Camera et al., *Euclid preparation. Cosmology likelihood for observables in euclid (CLOE). 3. Inference and forecasts*, .
- [29] J. Green, P. Schechter, C. Baltay, R. Bean, D. Bennett, R. Brown et al., *Wide-field InfraRed survey telescope (WFIRST) final report*, Aug., 2012. 10.48550/arXiv.1208.4012.
- [30] Q. Xiong, Y. Gong, X. Zhou, H. Lin, F. Deng, Z. Li et al., *Cosmological forecast for the weak gravitational lensing and galaxy clustering joint analysis in the CSST photometric survey*, Oct., 2024.
- [31] H. Miao, Y. Gong, X. Chen, Z. Huang, X.-D. Li and H. Zhan, *Forecasting the BAO measurements of the CSST galaxy and AGN spectroscopic surveys*, .
- [32] Y. Song, Q. Xiong, Y. Gong, F. Deng, K.C. Chan, X. Chen et al., *Cosmological forecast of the void size function measurement from the CSST spectroscopic survey*, .
- [33] Y. Song, Q. Xiong, Y. Gong, F. Deng, K.C. Chan, X. Chen et al., *Cosmological prediction of the void and galaxy clustering measurements in the CSST spectroscopic survey*, .
- [34] H. Lin, Y. Gong, X. Chen, K.C. Chan, Z. Fan and H. Zhan, *Forecast of neutrino cosmology from the CSST photometric galaxy clustering and cosmic shear surveys*, *Monthly Notices of the Royal Astronomical Society* **515** (2022) 5743.
- [35] H. Lin, F. Deng, Y. Gong and X. Chen, *Constraining ultralight axions with CSST weak gravitational lensing and galaxy clustering photometric surveys*, *Mon. Not. Roy. Astron. Soc.* **529** (2024) 1542.
- [36] A. Chen, Y. Gong, F. Wu, Y. Wang and X. Chen, *Constraining Brans-Dicke cosmology with the CSST galaxy clustering spectroscopic survey*, *Research in Astronomy and Astrophysics* **22** (2022) 55021.
- [37] J.-H. Yan, Y. Gong, M. Wang, H. Miao and X. Chen, *Forecasting constraint on the  $f(R)$  theory with the CSST SN ia and BAO surveys*, *Research in Astronomy and Astrophysics* **24** (2024) 115013.
- [38] P. Collaboration, N. Aghanim, Y. Akrami, M. Ashdown, J. Aumont, C. Baccigalupi et al., *Planck 2018 results. VI. Cosmological parameters*, *Astronomy and Astrophysics* **641** (2020) A6.
- [39] B. Carr and J. Silk, *Primordial black holes as generators of cosmic structures*, *Monthly Notices of the Royal Astronomical Society* **478** (2018) 3756.
- [40] B. Carr, M. Raidal, T. Tenkanen, V. Vaskonen and H. Veermäe, *Primordial black hole constraints for extended mass functions*, *Physical Review D* **96** (2017) 23514.
- [41] N. Afshordi, P. McDonald and D.N. Spergel, *Primordial black holes as dark matter: the power spectrum and evaporation of early structures*, *Astrophysical Journal* **594** (2003) L71.
- [42] D. Inman and Y. Ali-Haïmoud, *Early structure formation in primordial black hole cosmologies*, *Physical Review D* **100** (2019) 083528.
- [43] A. Lewis, A. Challinor and A. Lasenby, *Efficient computation of cosmic microwave background anisotropies in Closed friedmann-robertson-walker models*, *Astrophysical Journal* **538** (2000) 473.

- [44] A. Mead, S. Brieden, T. Tröster and C. Heymans, *HMcode-2020: improved modelling of non-linear cosmological power spectra with baryonic feedback*, *Monthly Notices of the Royal Astronomical Society* **502** (2021) 1401.
- [45] D.N. Limber, *The analysis of counts of the extragalactic nebulae in terms of a fluctuating density field. II*, *Astrophysical Journal* **119** (1954) 655.
- [46] D.H. Weinberg, R. Davé, N. Katz and L. Hernquist, *Galaxy clustering and galaxy bias in a  $\lambda$ CDM universe*, *Astrophysical Journal* **601** (2004) 1.
- [47] D. Huterer, M. Takada, G. Bernstein and B. Jain, *Systematic errors in future weak-lensing surveys: requirements and prospects for self-calibration*, *Monthly Notices of the Royal Astronomical Society* **366** (2006) 101.
- [48] H. Hildebrandt, M. Viola, C. Heymans, S. Joudaki, K. Kuijken, C. Blake et al., *KiDS-450: cosmological parameter constraints from tomographic weak gravitational lensing*, *Mon. Not. Roy. Astron. Soc.* **465** (2017) 1454.
- [49] B. Joachimi, M. Cacciato, T.D. Kitching, A. Leonard, R. Mandelbaum, B.M. Schäfer et al., *Galaxy Alignments: An Overview*, *Space Science Reviews* **193** (2015) 1.
- [50] D. Foreman-Mackey, D.W. Hogg, D. Lang and J. Goodman, *emcee : the MCMC hammer*, *Publications of the Astronomical Society of the Pacific* **125** (2013) 306.
- [51] B. Carr and F. Kuhnel, *Primordial Black Holes as Dark Matter: Recent Developments*, *Annual Review of Nuclear and Particle Science* **70** (2020) 355.
- [52] N. Esser, C. Filion, S. De Rijcke, N. Kallivayalil, H. Richstein, P. Tinyakov et al., *Constraints on asteroid-mass primordial black holes in dwarf galaxies using Hubble Space Telescope photometry*, *Astronomy and Astrophysics* **698** (2025) A290.
- [53] Y. Ali-Haïmoud, E.D. Kovetz and M. Kamionkowski, *The merger rate of primordial-black-hole binaries*, *Physical Review D* **96** (2017) 123523.
- [54] S.V. Pilipenko, M.V. Tkachev and N.R. Arakelyan, *On the increase in the concentration of primordial black holes in the halos of dwarf galaxies*, .